REPORT DOCUMENTATION PAGE

Form Approved OMB No. 0704-0188

Public reporting burden for this collection of information is estimated to average 1 hour per response, including the time for reviewing instructions, searching existing data sources, gathering and maintaining the data needed, and completing and reviewing the collection of information. Send comments regarding this burden estimate or any other aspect of this collection of information, including suggestions for reducing the burden, to Department of Defense, Washington Headquarters Services, Directorate for Information Operations and Reports (0704-0188), 1215 Jefferson Davis Highway, Suite 1204, Arlington, VA 22202-4302. Respondents should be aware that notwithstanding any other provision of law, no person shall be subject to any penalty for failing to comply with a collection of information if it does not display a currently valid OMB control number.
PLEASE DO NOT RETURN YOUR FORM TO THE ABOVE ADDRESS.

1. REPORT DATE *(DD-MM-YYYY)* 21-11-2006	2. REPORT TYPE Final Report	3. DATES COVERED *(From – To)* 28 May 2003 - 24-Jul-07

4. TITLE AND SUBTITLE High Temperature Protonic Conductors by Melt Growth	5a. CONTRACT NUMBER FA8655-03-1-3040
	5b. GRANT NUMBER
	5c. PROGRAM ELEMENT NUMBER
6. AUTHOR(S) Professor Julián Martínez-Fernández	5d. PROJECT NUMBER
	5d. TASK NUMBER
	5e. WORK UNIT NUMBER

7. PERFORMING ORGANIZATION NAME(S) AND ADDRESS(ES) University of Seville Av/ Reina Mercedes s/n, Apdo. 1065 Seville 41080 Spain	8. PERFORMING ORGANIZATION REPORT NUMBER N/A

9. SPONSORING/MONITORING AGENCY NAME(S) AND ADDRESS(ES) EOARD PSC 821 BOX 14 FPO AE 09421-0014	10. SPONSOR/MONITOR'S ACRONYM(S)
	11. SPONSOR/MONITOR'S REPORT NUMBER(S) Grant 03-3040

12. DISTRIBUTION/AVAILABILITY STATEMENT

Distribution authorized to US Government agencies only, Adminstrative use, 23 Jun 2004. Other requests for this document shall be referred to the European Office of Aerospace Research and Development (AFMC), PCS 802 BOX 14, FPO, AE 09499-0014.

13. SUPPLEMENTARY NOTES

14. ABSTRACT

This report results from a contract tasking University of Seville as follows: The key goal of the proposed research is to produce a family of single crystal and multiphase materials that exhibit high temperature protonic conductance, and superior mechanical properties at elevated temperatures. The program will simultaneously pursue three broad, integrated objectives: (i) to develop directionally solidified high temperature protonic conductors, (ii) to formulate a microscopic model of the mechanical behavior that will elucidate the defect interaction and transport for this class of materials and related structures, and (iii) to correlate structure and conductance from the atomistic and electronic length scales. These will be accomplished in eight project tasks: fabrication of simple perovskites; fabrication of mixed perovskites; fabrication of duplex structures; microstructural characterization; mechanical properties; impedance spectroscopy; optimization of conductance in mixed perovskites/duplex structures; and, hydrogen profiling measurements.

15. SUBJECT TERMS
EOARD, Ceramics, Eutectic, Fuel Cells

16. SECURITY CLASSIFICATION OF:			17. LIMITATION OF ABSTRACT UL	18, NUMBER OF PAGES	19a. NAME OF RESPONSIBLE PERSON KEVIN J LAROCHELLE, Maj, USAF
a. REPORT UNCLAS	b. ABSTRACT UNCLAS	c. THIS PAGE UNCLAS		30	19b. TELEPHONE NUMBER *(Include area code)* +44 (0)20 7514 3154

Standard Form 298 (Rev. 8/98)
Prescribed by ANSI Std. Z39-18

HIGH TEMPERATURE PROTONIC CONDUCTORS BY MELT GROWTH

Final Report FA8655-03-1-3040 (May 2005-May 2006)

PI: Julián Martínez Fernández
Departamento de Física de la Materia Condensada
University of Seville, Sevilla, SPAIN

High temperature protonic conductors (HTPC) were fabricated by solid-state sintering (polycrystals) and by melt processing by laser-heated floating zone method. Several families of compositions were selected: $SrCe_{1-x}M_xO_{3-\delta}$ (with M: Zr and Y; x = 0.1, 0.2), $BaCe_{1-x}M_xO_{3-\delta}$ (with Yb, Ca and Y; x = 0.05, 0.2), $Sr_3Ca_{1.18}Nb_{1.82}O_{9-\delta}$, $SrZr_{0.8}Y_{0.2}O_{3-\delta}$ and $SrTi_{0.95}Sc_{0.05}O_{3-\delta}$. The best processing routes were studied in depth. Their microstructure was studied by scanning and transmission electron microscopy, X-ray diffraction, and electron back scattering diffraction. Their mechanical properties have been studied by compression tests at constant load and constant compression rate.

Fabrication routes for high density polycrystalline HTPC have been developed. The relation between the processing, dopants, microstructure and mechanical properties is discussed. Understanding of plasticity is important to determine the ultimate component performance, and because its direct relationship to processing and transport. Preliminary data in electrical conductivity is presented.

Introduction

High temperature proton conductors (HTPC) have a great interest in an ample range of electrochemical applications, like for example in steam electrolyzers, solid state fuel cells, gas separation membranes, moisture sensors and high-density energy storage applications, among others (1-5). Since Iwahara et al. discovered the proton conducting properties on rare earth-doped $SrCeO_3$ (6), great effort has been put in developing novel perovskites with enhanced ionic and protonic conductivity (7, 8). Such perovskites, as $BaCeO_3$, $KTaO_3$ and $SrZrO_3$, have been found to be proton conducting when doped with trivalent ions occupying the B^{4+} sites in the perovskite ABO_3 structure (9-14).

In fact, many studies have been performed on structure, defect chemistry, conductivity, processing and consolidation of doped $SrCeO_3$ and $BaCeO_3$ compounds (1-6, 9-23). Nevertheless, few studies have been focused in the high temperature mechanical properties of these protonic conducting materials, despite the importance of this information to processing and ultimate component performance. In addition, this studies can contribute information on the diffusion processes taking place in these materials, which are of great importance in the sintering.

The laser-heated floating zone (LHFZ) method is a fast technique that produces nearly defect-free materials in a variety of processing conditions and shapes (24-26). Depending on the solidification geometry, fibres and rods with diameters ranging from 200 μm to 4 mm can be produced. One of the main advantages of this technique is that it is almost contamination-free, as the molten zone is never in contact with a crucible and does not need another material acting as a support for the melt. This processing method produces very high thermal gradients within the sample, which are responsible for some of the novel microstructural features attainable (27). In particular, it is possible to obtain highly textured materials with controlled microstructures by variation of the process parameters. Finally, this technique provides materials with improved mechanical and thermal stability up to nearly the melting temperature (28).

This work tries to give some light in this subject, comparing the relation between the processing, dopants, microstructure and mechanical properties of several families of compositions. $SrCe_{1-x}M_xO_{3-\delta}$ (with M: Zr and Y; x = 0.1, 0.2), $BaCe_{1-x}M_xO_{3-\delta}$ (with M: Yb, Ca and Y; x = 0.05, 0.2), $Sr_3Ca_{1.18}Nb_{1.82}O_{9-\delta}$, $SrZr_{0.8}Y_{0.2}O_{3-\delta}$ and $SrTi_{0.95}Sc_{0.05}O_{3-\delta}$ were fabricated in polycrystalline (by solid-state sintering) and melt grown crystals (by laser-heated floating zone method) form. Additionally this work is aimed to demonstrate the possibility of fabricating HTPC by the LHFZ method and to illustrate the microstructural, mechanical and conductivity advantages of the material produced over the polycrystalline material produced by sintering techniques.

During this one year period the research has been focused in the development of processing routes to fabricate polycrystals with high density and homogeneous composition, and the study of their microstructure and properties, as well as to develop understanding on the single crystals properties obtained in previous years.

Experimental methods

Solid-state sintering

Starting materials were commercially available BaO (99.99 % pure), CeO_2 (99 % pure) and Yb_2O_3 (99.9 % pure) powders adquired to Sigma-Aldrich. The chemicals, mixed in a stoichiometric ratio to yield the composition $BaCe_{1-x}Yb_xO_{3-\delta}$, in particular, with x = 0.05, 0.2, were ball-milled (WC ball and bottle) for 5 min. The resulting slurry was then dried at 70 ºC. The dried powders were heated 1000 and 1200 °C for 1 h. They were examined by X-ray powder diffraction analysis (Philips X-Pert, provided with high-temperature chamber, until 1200 ºC). Simultaneous thermogravimetric and differential thermal analysis (TGA, DTA) were carried out at a heating rate of 10 °C/min. in air, using a thermal analyser (Seiko instruments, Inc, model TG/DTA 6300). After calcining at 1200 °C for 1 h, the powders were ground with an agate mortar, and then ball-milled in dry air for 30 min. to disperse agglomerates. Compacts were obtained by pressing uniaxially the ball-milled calcined powders, without adding binders, at 100 MPa for 30 s and isostatically at 200 MPa for 3 min. at room temperature. The green density was ~70 % of relative density.

Subsequent sintering of pellets was carried out on a zirconia plate, in alumina crucibles, in air at 1500 °C for 10 hours. Bulk density were measured by the Archimedes method using carbon tetrachloride as the liquid medium. Around 85 % of relative density

was obtained. The sintered speciments were polished on SiC paper and diamond paste down to a grain size of 0.25 μm. The phases present in the samples were identified by X-Ray diffraction (XRD).

Parallelly, the process was repeated using $BaCO_3$ as precursor. A relative density of 94 % was obtained, after sintering to 1500 ℃ for 10 hours. It's obtained also a uniform distribution of the elements in the sample. Finally, it was tried to optimize the processing of polycrystals using BaO, diminishing the size of particle of precursors powders and calcining to smaller temperature. Sintering to 1700 ℃ was necessary during 10 hours to obtain relative densities superior to 95 %. On the other hand, the sintering produced lost of barium and the segregation of dopants.

After solid-state sintering, rectangular parallelepipeds ~2×2×4 mm were cut from the sintered follow pellets with a low-speed diamond saw and to be used for mechanical testing.

The rest of the compositions were produced following the same route.

Crystal growth

The crystals have been grown using the LHFZ method described elsewhere (27, 29, 30). A CO_2 laser was focused onto a polycrystalline precursor feed bar to establish a reduced molten zone, which was held in place by liquid surface tension. All the samples have been grown in NASA-Glenn Research Center using a travel rate of 500 mm/h without rotation, except the doped $BaCeO_3$ that was grown in ICMA (Zaragoza, Spain) at 300 mm/h and a rotation rate of 50 revolutions per minute. The complete process was performed in air.

After the LHFZ process, cylinders with a typical length of 50-100 mm and a diameter ranging from 3 to 4 mm were obtained. The diameter was quite irregular due to the high evaporation rate of the oxides that was observed during the melt growth. Finally, cylindrical samples of 4-5 mm in length were cut with a low-speed diamond saw and used to test deformation.

Microstructural characterization and high temperatures mechanical properties

The microstructural evolution studies and chemical analysis were performed by scanning and transmission electron microscopy (SEM, TEM) and energy-dispersive X-Ray spectrometry (EDS). Transverse and longitudinal sections of the different samples were cut using a low-speed diamond saw and polishing using diamond paste up to a grain size of 0.25 μm. SEM and EDS observations were carried out in a Philips XL-30 SEM y HITACHI S5200 HRSEM. TEM specimens were prepared using a standard procedure. The observations were carried out in a Hitachi H800 TEM and Philips CM200 TEM. Due to the good electronic conductivity of this samples no conductive coating was needed.

High temperatures mechanical properties were studied by compression tests (Microtest EM1/50/FR, Madrid, España) under constant strain rate and constant load conditions in high-purity Ar and air atmospheres for temperatures up to 1350 ℃.

Ionic conductivity

The ionic conductivity of the material was studied from 145ºC to 995ºC in air at intervals of 50 ºC using the technique of electrochemical impedance spectroscopy (CIEMAT, Spain, in collaboration with Hynergreen S.L.). The electrolyte samples have been painted with platinum by both faces, in order to improve the electrical contact, and they were placed between two platinum electrodes. The impedance measurement were made with a system Autolab (Eco Chemie B.V.). An amplitude of signal of 5 mV was applied in a range of frequencies of 1 MHz to 10 mHz, with 8 points per decade to open circuit.

Results and discussion

Fabrication

In order to fabricate Yb-doped $BaCeO_3$ the powder derived from mixing BaO, CeO_2 and Yb_2O_3 was heated to 1000 and 1200 °C for 1 hour at 5 °C/min, and the products were identified with XRD. Initially, starting materials were present, at 400 ºC appeared the intermediate compound $Yb_{0.2}Ce_{0.8}O_{1.9}$ and when the temperature was raised to 800 ºC, the solid-state reaction was initiated, and diffraction peaks belonging to $BaCe_{0.8}Yb_{0.2}O_{3-\delta}$, appeared. As the firing temperature was raised more, $BaCe_{0.8}Yb_{0.2}O_{3-\delta}$ was formed in the products, with a corresponding decrease in BaO and CeO_2. The formation of $BaCe_{0.8}Yb_{0.2}O_{3-\delta}$, was completed when the temperature reached 1000 ºC, and no BaO, CeO_2, Yb_2O_3 and $Yb_{0.2}Ce_{0.8}O_{1.9}$ phases could be detected, as illustrated in figure 1.

Simultaneous DTA-TGA was used in analysing the formation of doped $BaCeO_3$. The result of the $BaCe_{0.95}Yb_{0.05}O_{3-\delta}$ is shown in figure 2. A small amount of weight loss occurred in the low temperature range, that one corresponds with the water elimination. Between 400-500ºC it's observed a new loss, that corresponds with the decomposition of the hydroxides of barium formed, detected by XRD examination. The last weight loss begins at 800 ºC and stays until over 1000 ºC. DTA curve indicates an exothermic side which is associated with the formation of ternary oxide, as indicated by the XRD examination. The rest of compositions shows a similar behavior.

The figure 3 shows the semi-quantitative EDS analysis of a sample sintered at 1500 ºC using BaO as precursor, after sintering at 1700 ºC, and one made using $BaCO_3$ as precursor and sintered at 1500 ºC. The loss of stoichiometrical in the sample sintered at 1700 ºC is clear.

Microestructural characterization

The figure 4 show a SEM-TEM micrographs of polycrystal $BaCe_{0.95}Y_{0.05}O_{3-\delta}$ sintered at 1500 ºC for 10 hours. It's observed the porosity of the material and a size of micrometric grain. The diffraction patterns show that the grains are crystalline and the intergranular phase amorphous.

Figures 5 and 6 show the detail of the processing routes together with the microstructures obtained. Figure 7 shows the dependence of the precursors, processing route and sintering temperature with the final density. The processing route in which the $BaCO_3$ is used as precursor gives the best materials, because the materials with slightly higher density, obtained in the processing route in which the BaO is used as precursor, show a lower Ba content due to evaporation.

The particle size of precursors and ternary compound were measured and are shown in Figure 8. A low particle size is maintained because the milling after each fabrication step.

In figure 9 the solidification front of directionally solidified $BaCe_{0.95}Y_{0.05}O_{3-\delta}$ by LHFZ method can be seen. In the left zone the polycrystalline precursor is observed, in the right the melt grown crystal. A concave front of solidification is observed and how the porosity directional concentrates and disappears when melting the material. The detail shows the interior of a pore in the molten zone frozen by switching off the laser. The grain growth is clear, if compared with figure 4.

The directionally solidified materials presented a unique microstructure, with characteristic intermediate between single crystals and polycrystals, consisting of strongly textured cells with an intercellular amorphous phase with low Ce or Ba content (Fig. 11,12, and 13). A representation of this microestructure is shown in figure 10. Cell's internal microstructure consisted of domains originating from oxygen octahedral tilting with Pnma structure (28, 29, 31). On the other hand, the average volume of the unit cells decrease with dopant content in $SrCe_{1-x}Y_xO_{3-\delta}$ because the increase of vacancies, overcoming the effect of the difference in ionic radius between Ce^{4+} and Y^{3+} (29, 32) (Fig. 14). The same effects occurs in $BaCe_{1-x}Y_xO_{3-\delta}$ (33).

Mechanical properties: strength

Previous investigations showed that the high temperature mechanical properties of the directionally solidified materials (Fig. 15 and 16) were superior to the preliminary data obtained in polycrystalline HTPC, and could be further improved by a reduction of the intercellular phase (28, 31). The extensive data obtained in the polycrystals with a broad range of compositions corroborate its lower strength compared to directionally solidified materials (Fig. 17-19). In polycrystals the plastic deformation starts to be significant around 1000 $^{\circ}$C (Fig. 17).

The factor determining ther strength/hardening, the amount of intercellular phase together with the dopant ionic radius, concentration and charge, were studied in detail. Figure 20 shows how the strength increases with ionic radius difference (B^{4+}-dopant). Figure 21 shows how the strength increase with composition of 3+ dopants (Y^{3+} and Yb^{3+}), i.e., the effect of ionic radius that causes lattice deformation, dominates over the creation of complex defects involving vacancies that tent to cancel this deformation:

$$[Y'_{Ce} - V_O^{\bullet\bullet}]^{\bullet}$$
$$[Y'_{Ce} - V_O^{\bullet\bullet} - Y'_{Ce}]$$

On the other hand, the strength decrease with composition of 2+ dopant. Therefore, the formation of complex defects dominate over the effect of ionic radius in this case due to the larger amount of oxygen vacancies created:

$$[Ca''_{Ce} - V_O^{\bullet\bullet}]$$

Mechanical properties: plastic behaviour

The creep behaviour of the directionally solidified systems can be well described using two different deformation regimes. A primary regime, where the strain rate decreases with strain, and the stress exponent n depends both on stress and strain. The stress exponent is meaningless in this regime, as suggests the fact that non physical ($n < 0$) values are obtained for some stresses.

This behaviour can be explained taking into account the redistribution of the intercellular amorphous phase, and assuming that viscous flow plays a role at low strains. To model this behaviour Dryden and Wilkinson [35] proposed a viscous flow model in which the strain rate of the intercellular phase is linear with stress. Refinements of this model by Martinez et al. [36] showed that strain rate must decrease following the equation :

$$\frac{d\varepsilon_z}{dt} = \frac{\sigma_z}{\eta} \left[\frac{1}{\gamma \left(\frac{h}{d} - \varepsilon_z \right)^3} + \frac{4}{\left(\frac{2h}{d} + \varepsilon_z \right)^3} \right]^{-1}$$

where η is the amorphous phase viscosity, d is the mean cell size; h is the amorphous phase thickness and γ is a cell form factor.

This equation explains the continuous decrease in $\dot{\varepsilon}$ with the applied stress as shown in Figure 22. The decrease rate (the slope of the curve the figure) increases with increasing stress or temperature. This would account for the n < 0 stress exponent observed.

It was showed, using EBSD measurements, that a rigid rotation of the cells occurred during primary creep (Fig. 23). At the test temperatures the cells can rotate rigidly without deforming and the strain is accommodated by a redistribution of the amorphous phase, which flows out of the sample. The cells will eventually touch each other during this process up to the point that they can not rotate anymore, and deformation of the cells is necessary for macroscopic plastic deformation. At this point the stationary deformation regime is activated and cell coalescence occurs easily because

of their close crystallographic orientation. The deformation mechanism would have then a contribution of Nabarro-Herring creep.

We can write the phenomenological creep equation for $Sr_3Ca_{1.18}Nb_{1.82}O_{9-\delta}$ in the steady creep regime as:

$$\dot{\varepsilon} = A\sigma^{1.9 \pm 0.2} \exp\left[\left(-670 \pm 94\,\text{kJ/mole}\right)/RT\right]$$

The value of the stress exponent, $n \sim 2$ suggests a mixed diffusional/dislocation driven creep mechanism. The strain rate can be written in this case as:

$$\dot{\varepsilon} = A\sigma + B\sigma^{n'}; A = \frac{\alpha D_l \Omega}{d^2 kT}$$

where $A\sigma$ is the bulk diffusion contribution, $B\sigma^{n'}$ the dislocation contribution to plasticity, α is a constant that depends on the diffusional creep mechanism, D_l is the diffusion coefficient, Ω the atomic volume, d is the characteristic length of the microstructure, k is the Boltzmann constant, and T the temperature.

We can relate the measured stress exponent (n) with the contribution to plasticity of diffusion and dislocations:

$$n = \frac{\partial \ln \dot{\varepsilon}}{\partial \ln \sigma} = 1 + \frac{(n'-1)B\sigma^{n'}}{A\sigma + B\sigma^{n'}}$$

Taking n = 1.9, and n' = 3-5 (stress exponent corresponding to a pure dislocation mechanism), the ratio of contribution to plasticity of bulk-diffusion and dislocation can be estimated. For our experimental result, a contribution of 20 % - 40 % [$B\sigma^{n'}/(A\sigma + B\sigma^{n'})$=0.2-0.4] of dislocations to plastic strain is estimated depending on the diffusional mechanism considered.

Following the previous considerations, the diffusion coefficient for $Sr_3Ca_{1.18}Nb_{1.82}O_{9-\delta}$ can be estimated from the creep data. The results are shown in the Figure 24, compared with the results for $BaCe_{0.8}Y_{0.2}O_{3-\delta}$ obtained by Goretta et al. [23].

In polycrystals, the stress exponents is very close to one (23) (Fig. 25), and the grain growth is clear after the mechanical tests (Fig 26), indicating the dominance of diffusional mechanisms in plastic deformation.

Ionic conductivity

Figure 27 shows the Nyquist's diagrams obtained with the electrolyte 20Y:BaCeO$_3$ at different temperatures. It's observed a diminution of the impedance when increasing the temperature. The Nyquist's diagrams present two arcs clearly (329 °C, Fig.27c) that probably correspond to the resistance of grain boundary (R_{gb}) and polarization of the electrodes (or interphase electrolyte/electrode), respectively. The point of cut with the X-axis is attributed to the inner grain resistance (R_b). When increasing the temperature, the resistance of the interphase and the electrolyte ($R_{gb}+R_b$) decreases, which causes the disappearance of the first arc and it only appears the arc associated to the processes of the

electrode (Fig.9 d, e). For temperatures lower than 600 ºC, the resistance of the electrolyte ($R_{gb}+R_b$) is inferior to the polarization resistance (Ri), whereas to temperatures superior to 600 ºC, interphase resistance is become much smaller than the electrolyte resistance. This implies that the interphase resistance associated to the processes of the electrode will be a critical parameter in the operation of fuel cells with $20Y:BaCeO_3$ electrolyte ay low temperature.

Total conductivity of the electrolyte, for each temperature, was calculated from the total resistance of the electrolyte (inner grain resistance + resistance of grain boundary), using the equation:

$$o_i = \frac{l}{sR_i}$$

(1)

where l is the thickness of the sample, and S the area of the electrode of the surface of the sample.

Figure 28 and shows the conductivity of $20Y:BaCeO_3$ versus temperature. The compound $20Y:BaCeO_3$ presents an ionic conductivity in air, and even higher than some conductivities in H_2 (Figure 29). These results also corroborate the good quality of the polycrystals fabricated in this work.

Conclusions

Perovskites HTPC were successfully fabricated by solid-state sintering and by melt growth using the laser heated floating zone method. The single-phase perovskite was formed on T > 1000 ºC. The polycrystalline samples have a microstructure formed of grains of micrometric size an with final densities over 95%. The directionally solidified materials have unique microstructure, with characteristic intermediate between single crystals and polycrystals.

The high temperature mechanical properties of the directionally solidified materials are superior to those of polycrystalline HTPC. In polycrystals the stress exponents are very close to one and the plastic deformation causes grain growth, indicating the dominance of diffusional mechanisms. For the directionally solidified materials, the mechanism that controls plasticity is grain rotation associated with redistribution of the intercellular phase, accommodated by cell coalescence, due to diffusion/dislocations. In addition, differences in dopant ionic radius and valence with the host atom influence strength. A larger difference in ionic radius increase strength because of cell distortion. A larger difference in valence decrease strength with dopant amount because of complex defect formation.

The electrical conductivity in air of these polycrystals is very promising, being in the high region of the literature values of conductivity in air.

Acknowledgments

References

1. B. C. Steele. *Solid State Ionics*, **86-88**, 1223 (1996).
2. T. Hagawa, K. Moe, T. Hiramatsu and S. Goto. *Solid State Ionics*, **106**, 227 (1998).
3. C. H. Chen, H. J. M. Bouwmeeste, R. H. E. van Doorn, H. Kruidhof and A. J. Burggraaf. *Solid State Ionics*, **98**, 7 (1997).
4. I. Kosacki and H.U. Anderson. *Applied Physics Letters*, **69**, 4171 (1996).
5. J. Guan, S. E. Dorris, U. Balachandran and M. Liu. *Solid State Ionics*, **100**, 45 (1997).
6. H. Iwahara, T. Esaka, H. Uchida and N. Maeda. *Solid State Ionics*, **3/4**, 359 (1981).
7. H. Iwahara, *Cambridge Univ. Press*, 122 (1992).
8. H. Iwahara, H. Uchida and S. Tanaka. *Solid State Ionics*, **9/10**, 1021 (1983).
9. H. Iwahara, T. Yajima and H. Uchida, *Solid State Ionics*, **70/71**, 267 (1994).
10. H. Uchida, N. Maeda and H. Iwahara, *Solid State Ionics*, **11**, 117 (1983).
11. K. C. Liang and A. S. Nowick, *Solid State Ionics*, **61**, 77 (1993).
12. A. S. Nowick and Y. Du, *Solid State Ionics*, **77**, 137 (1995).
13. U. Reiche, R. R. Arons and W. Schilling, *Solid State Ionics*, **86–88**, 639 (1996).
14. G. Ma, H. Matsumoto and H. Iwahara, *Solid State Ionics*, **122**, 237 (1999).
15. H. Uchida, N. Maeda and H. Iwahara. *J. Appl. Electroch.*, **12**, 645 (1982).
16. J.F. Liu and A.S. Nowick, *Solid State Ionics*, **50**, 131 (1992).
17. N. Bonanos, *Solid State Ionics*, **53-56**, 967 (1992).
18. N. Taniguchi, K. Hatoh, J. Niikura and T. Gamo, *Solid State Ionics* **53-56**, 998 (1992).
19. N. Bonanos, B. Ellis, K.S. Knight and M.N. Mahmood, *Solid State Ionics*, **35**, 179 (1989).
20. N. Bonanos. *J. Phys. Chemis. Sol.*, **54**, 867 (1993).
21. S. D. Flint, M. Hartmanova, J. S. Jones and R. C. T. Slade, *Solid State Ionics*, **86-88**, 679 (1996).
22. Y.-M. Chiang, E.B. Lavik, I. Kosacki, H.L. Tuller and J.Y. Ying, *Appl. Phy. Let.*, **69**, 185 (1996).
23. K.C. Goretta, E.T. Park, J. Guan, U. Balachandran, S.E. Dorris and J.L. Routbort, *Solid State Ionics*, **111**, 295 (1998).
24. H. Sayir, S. C. Farmer, P. Lagerlof and A. Sayir, *Am. Cer. Soc.*, 53–63 (1994).
25. A. Sayir, S. C. Farmer, P. O. Dickerson and H. M. Yun, *Mater. Res. Soc. Symp. Proc.*, **365**, 21 (1995).
26. A. Sayir and S. C. Farmer, *Acta Mater.*, **48**, 4691 (2000).

27. J.I. Peña, R.I. Merino, N.R. Harlan, A. Larrea, G.F. de la Fuente and V.M. Orera. *J. Eur. Cer. Soc.*, **22**, 2595 (2002).

28. M.J. López Robledo, A.R. Pinto Gómez, J. Martínez Fernández, A.R. de Arellano López, A. Sayir. *Bol. Soc. Esp. Cer. y Vid.* **43-4**, 753 (2004).

29. J. Ramírez-Rico, M.J. López-Robledo, A. R. de Arellano-López, J. Martínez-Fernández and A. Sayir, *J. Eur. Cer. Soc.*, (2006). In Press. Available on line. doi:10.1016/j.jeurceramsoc.2005.12.003

30. G.F. de la Fuente, J.C. Díez, L.A. Angurel, J.I. Peña, A. Sotelo, R. Navarro, *Adv. Mater.*, **7**, 853 (1995).

31. M.J. López Robledo, J. Ramírez Rico, J. Martínez Fernández, A. R. de Arellano López, A. Sayir. *Bol. Soc. Esp. Cer. y Vid.* **44-5**, 347 (2005).

32. R. J. Phillips, N. Bonanos, F. W. Poulsen, E.O. Ahlgren, *Solid State Ionics*, **125**, 389 (1999).

33. K. Takeuchi , C. K. Loong, J. W. Richardson Jr., J. Guan, S.E. Dorris, U. Balachandran, *Solid State Ionics*, **138**, 63 (2000).

34. M.J. López Robledo, A.R. de Arellano López, J. Martínez Fernández, A. Sayir, *Solid State Ionics* Ref. **SSI-D-06-00075** (2006). In print.

35. J. R. Dryden, D. S. Wilkinson. *Acta Materialia* **45** (1997), p. 1259.

36. J. Martínez-Fernández, A. Muñoz, A.R. de Arellano López, F.M. Valera- Feria, A. Domínguez-Rodríguez, M. Singh. *Acta Materialia* **51** (2003), p. 3259.

Publications (May 2005- May 2006)

M. J. López-Robledo, J. Ramírez-Rico, A. R. De Arellano-López, J. Martínez-Fernández, A. Sayir. "Fabrication and microstructure of directionally solidified $SrCe_{1-x}Y_xO_{3-\delta}$ (x=0.1, 0.2) High Temperature Proton Conductors".
doi:10.1016/j.jeurceramsoc.2005.12.003
Journal of the European Ceramic Society Volume 26, Issue 16 , Pages 3705-3710 (2006).

J. Ramírez-Rico, M.J. López-Robledo, J. Martínez-Fernández, A.R. de Arellano-López, A. Sayir. "Microestructura y Comportamiento Plástico de Perovsquitas Conductoras Protónicas de Alta Temperatura". Bol. Soc. Esp. Cer. y Vid. 44-5, 347 (2005).

M.J. López-Robledo, A.R. de Arellano-López, J. Martínez-Fernández and A. Sayir
"Diffusion and creep of $Sr_3(Ca_{1.18}Nb_{1.82})O_{9-\delta}$ mixed Perovskite fabricated by melt processing"
Solid State Ionics Ref. SSI-D-06-00075 (2006). In print.

M. J. López-Robledo, J. Martínez-Fernández, A. R de Arellano-López,
C. Real-Pérez, J. I. Peña, and A. Sayir
"Fabrication and Properties of High Temperature Proton Conducting Perovskites"
Electrochemical Society Transactions, 3 (1) 459-469 (2006).

Presentation in conferences

"Fabricación y Microestructura de Conductores Protónicos de Alta Temperatura Crecidos por Fusión de Zona Flotante". VII Reunión Nacional y VI Conferencia Iberoamericana (Electrocerámica 2005).

"Fabricación de $BaCe_{1-x}M_xO_{3-\delta}$ (M: Y, Ca e Yb) por reacción en estado sólido"
M.J. López Robledo, C. Real Pérez, J. Martínez Fernández, A. Ramírez de Arellano López
XLVI Congreso de la Sociedad Española de Cerámica y Vidrio, Vall d'Alba, october 2006 .

"Fabrication and Properties of High Temperature Protonic Conductors"
2006 Joint International Meeting 210th Meeting of The Electrochemical Society XXI Congreso de la Sociedad Mexicana de Electroquimica Co-sponsored by the Sociedad Iberoamericana de Electroquimica Cancun, Mexico October - November, 2006

FIGURES
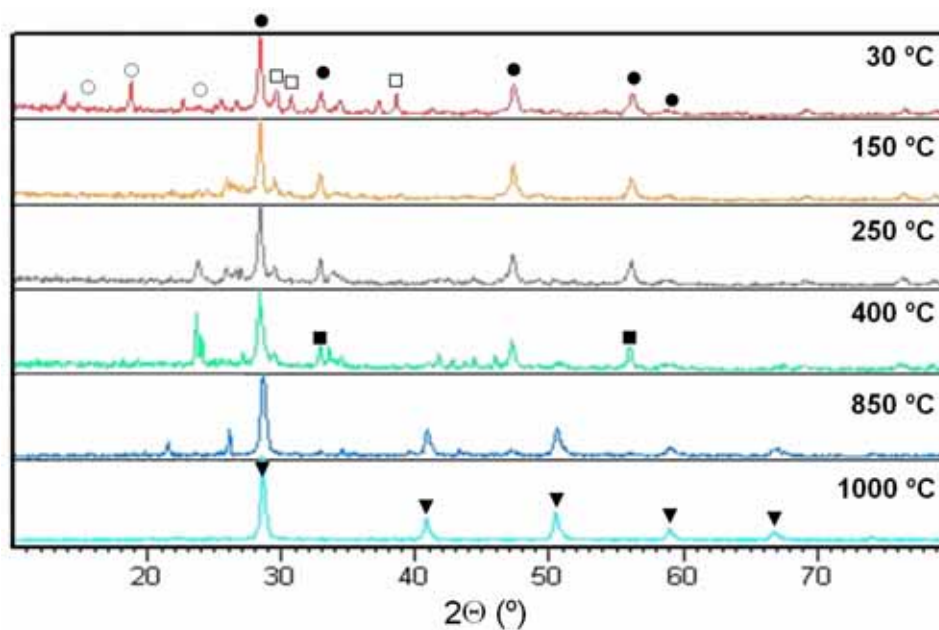
Figure 1. X-ray diffraction patterns of the mixture of $BaO \cdot 0.8CeO_2 \cdot 0.1Yb_2O_3$ heated at each temperature for 30 min. Symbols: ($\circ$) $Ba(OH)_2 \cdot H_2O$, ($\bullet$) CeO_2 and BaO, ($\square$) Yb_2O_3, ($\blacksquare$) $Yb_{0.2}Ce_{0.8}O_{1.9}$ and ($\blacktriangledown$) perovskite $BaCe_{0.8}Yb_{0.2}O_3$.
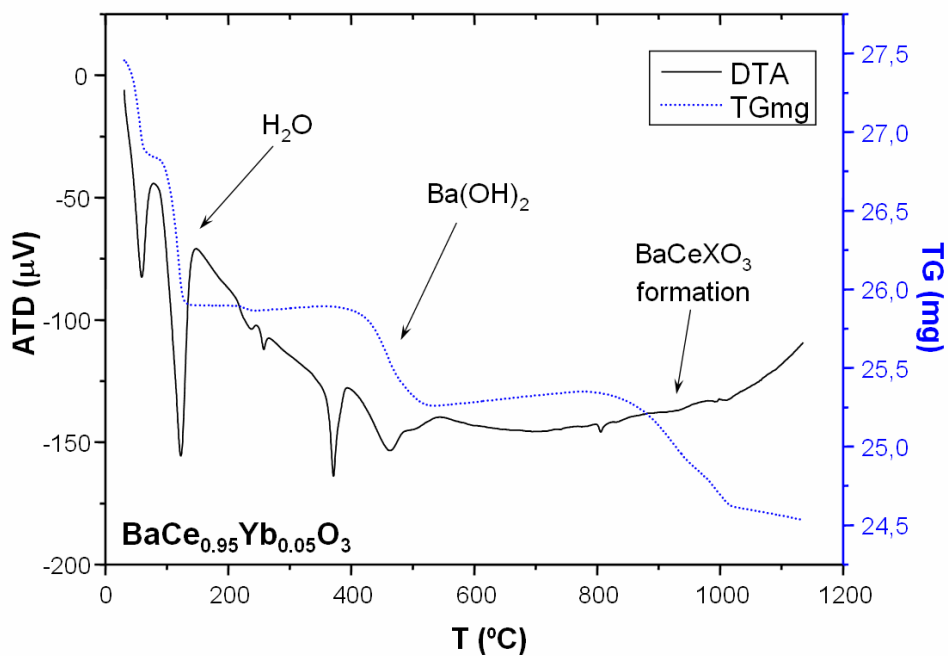
Figure 2. Thermogravimetric analysis (TGA) and differential thermal analysis (DTA) curves of the mixture of $BaO \cdot 0.95CeO_2 \cdot 0.025Yb_2O_3$.

20Y:BaCeO₃ using BaO and sintering to 1500 ºC for 10h			
% Wt	20Y:BaCeO₃ edge	20Y:BaCeO₃ center	Theoretician
Al_k	-	0,4 ± 0,1	-
Ba_L	45,6 ± 0,4	46,3 ± 0,4	43,6
Ce_L	34,5 ± 0,4	34,9 ± 0,4	35,6
Y_L	5,6 ± 0,4	4,8 ± 0,4	5,6
O_k	14,3 ± 0,4	13,6 ± 0,4	15,2

5Yb:BaCeO₃ using BaO and sintering to 1700 ºC for 10h			
% Wt	5Yb:BaCeO₃ general	5Yb:BaCeO₃ segregated	Theoretician
Al_k	1,2 ± 0,2	6,5 ± 0,2	-
Ba_L	48,1 ± 0,5	22,4 ± 0,5	46,8
Ce_L	48,8 ± 0,5	57,3 ± 0,5	45,4
Yb_L	1,9 ± 0,3	14,2 ± 0,3	2,9

20Yb:BaCeO₃ using BaCO₃ and sintering to 1500 ºC for 10h			
% Wt	20Yb:BaCeO₃ edge	20Yb:BaCeO₃ center	Theoretician
Al_k	4,4 ± 0,4	3,5 ± 0,4	-
Ba_L	41,5 ± 0,4	41,8 ± 0,4	41,4
Ce_L	35,9 ± 0,4	34,5 ± 0,4	33,8
Yb_L	13,0 ± 0,4	10,4 ± 0,4	14,5
O_k	5,2 ± 0,4	9,7 ± 0,4	10,4

Figure 3. Semi-quantitative EDS analysis of some sintered samples. Note: lines M of ytterbium agree with lines K of aluminium, reason why the composition of both can vary.
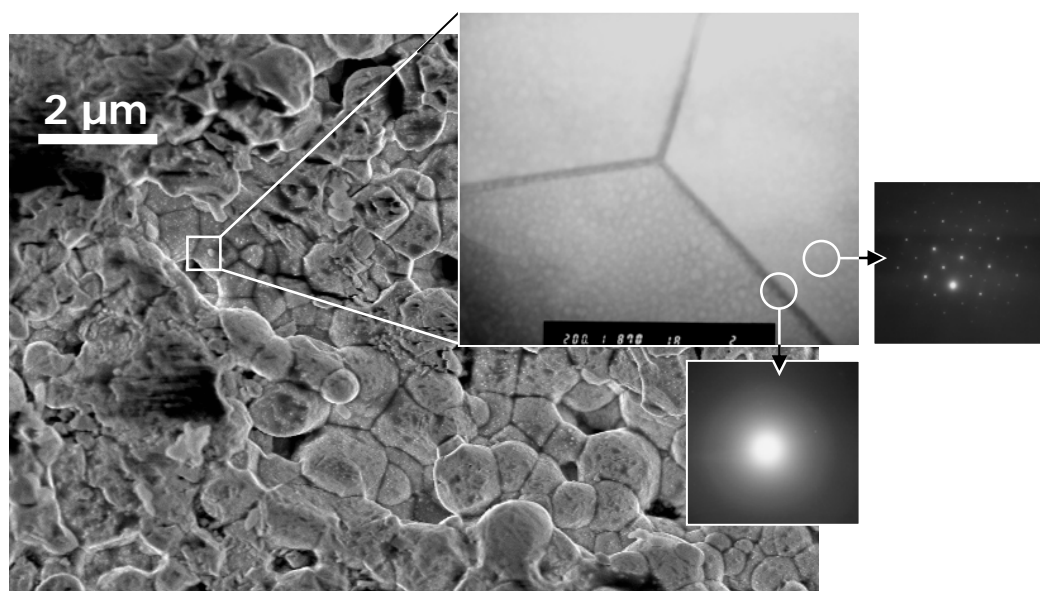
Figure 4. Scanning and transmission electron micrographs of polycrystal $BaCe_{0.95}Y_{0.05}O_{3-\delta}$ sintered at 1500 ºC for 10 hours.

*Samples with **BaO** as precursor*

✓ **Homogenous mixture of oxides milled previously 1h in dry:**

1 mol BaO + (1-x) mol CeO$_2$ + x/2 mol M$_2$O$_3$ → BaCe$_{(1-x)}$M$_x$O$_{3-\delta}$

✓ **Milling with centrifugal mill of agate in dry.**

✓ **Calcination to 1000 ºC 10 hour.**

✓ **Milling with centrifugal mill of agate in ethanol for 49 h.**

✓ **Pre-compacted uniaxial to 100 MPa during 30 s.**

✓ **Compacted isostatic to 200 MPa during 3 min.**

Sintering to 1500 ºC during 10 hours → 85 % of relative density and homogenous distribution of elements.

Sintering to 1700 ºC during 10 hours → >95 % of relative density, but there's segragación of dopants.
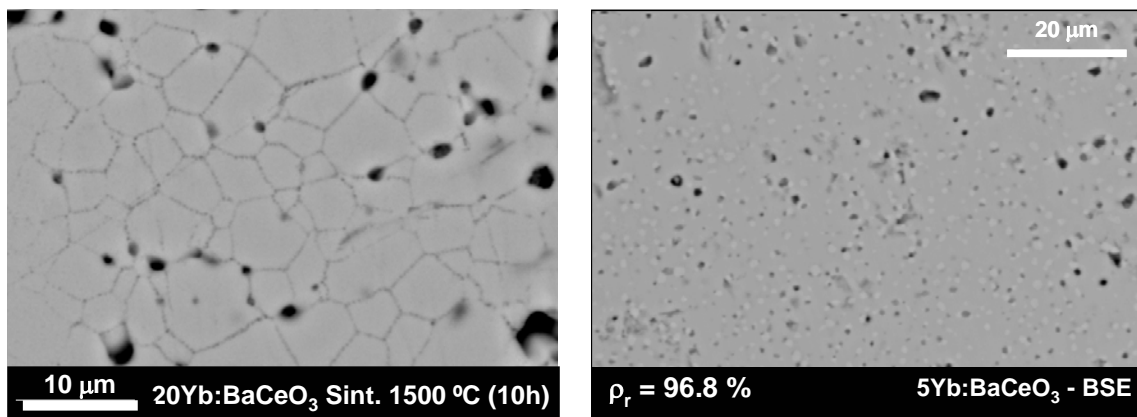
Figure 5 – Optimum fabrication process using oxides as precursors. The micrograph on the right correspond with the microstructure after sintering at 1500 °C, and the micrograph on the left correspond with the microstructure after sintering at 1700 °C

*Samples with **BaCO₃** as precursor*

✓ **Homogenous mixture of oxides:**

$$1 \text{ mol } BaCO_3 + (1-x) \text{ mol } CeO_2 + x/2 \text{ mol } M_2O_3 \rightarrow BaCe_{(1-x)}M_xO_{3-\delta} + CO_2\uparrow$$

✓ **Milling with centrifugal mill of agate in dry.**

✓ **Calcination to 1000 ºC 1 hour.**

✓ **Calcination to 1200 ºC 1 hour.**

✓ **Milling with centrifugal mill of agate in dry.**

✓ **Pre-compacted uniaxial to 100 MPa during 30 s.**

✓ **Compacted isostatic to 200 MPa during 3 min.**

✓ **Sintering to 1500 ºC during 10 hours → 94 % of relative density and** homogenous distribution of elements.
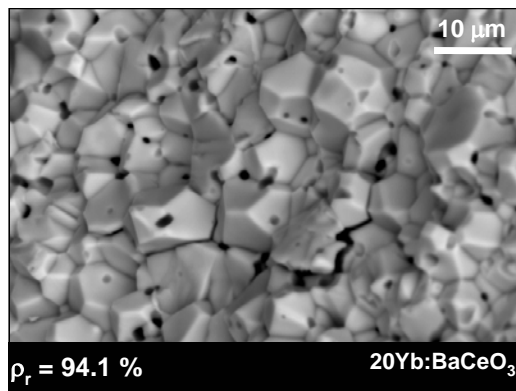
Figure 6 - Optimum fabrication process using BaCO₃ as precursor. The micrograph correspond with the microstructure after sintering at 1500 ºC
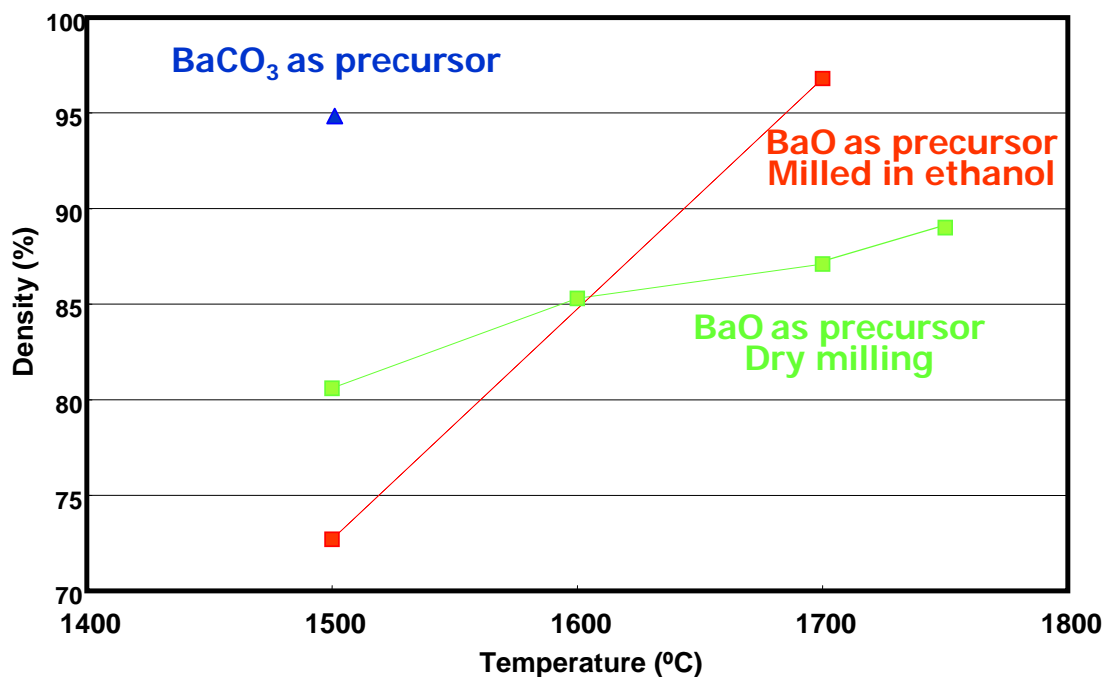
Figure 7 – Plot of final density as a function of the sintering temperature for the three processing routes.
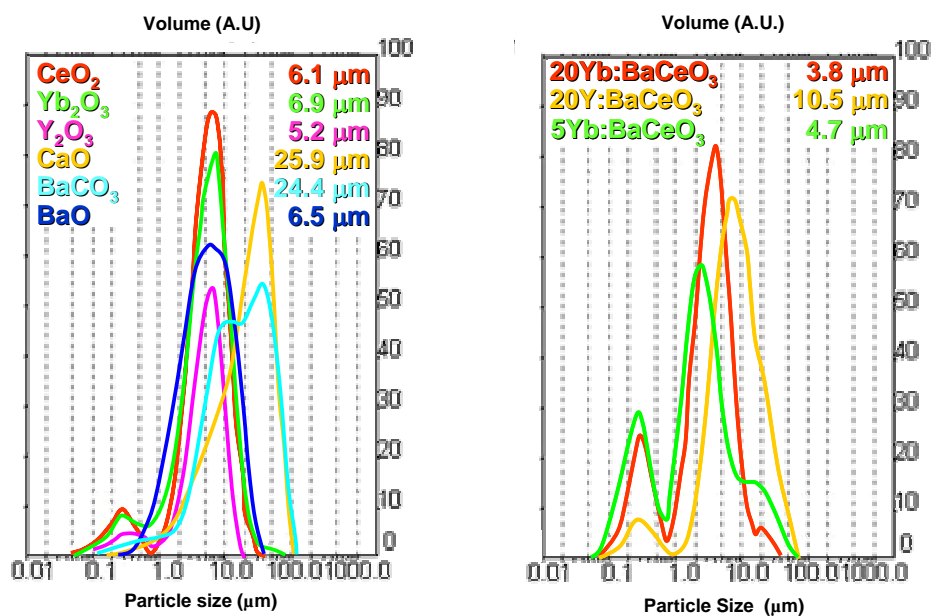
Figure 8 – Particle size of the precursors and final ternary compounds. The data of the ternary compound correspond with the solid state reaction using the oxides as precursors.
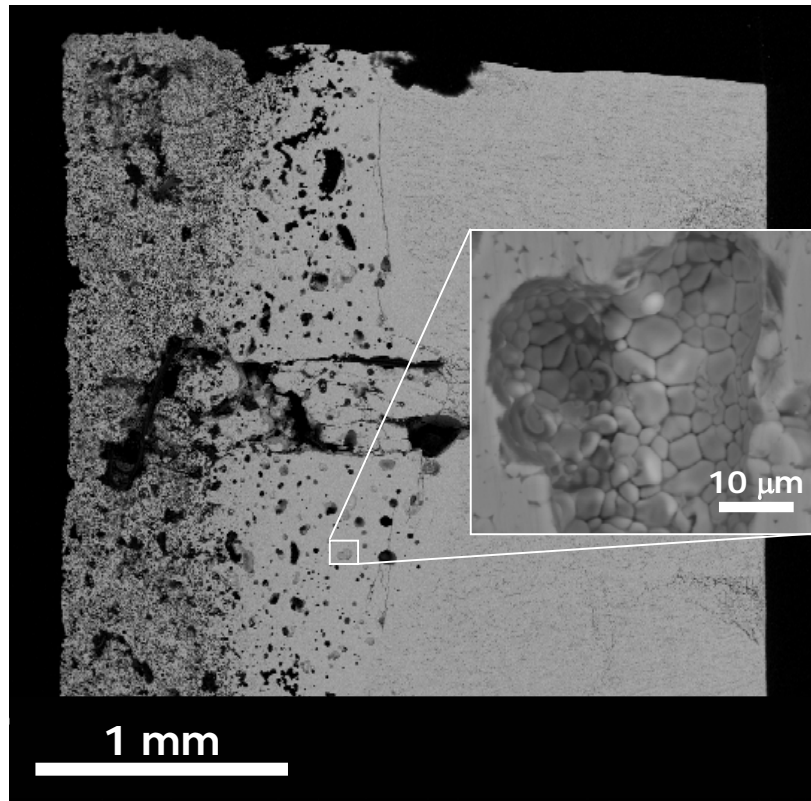
Figure 9. Scanning electron micrographs of the solidification front of directionally solidified $BaCe_{0.95}Y_{0.05}O_{3-\delta}$ by LHFZ method.
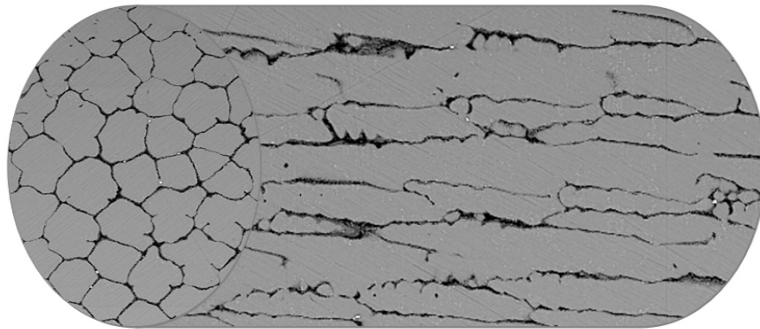
Figure 10. Virtual representation of the microestructure of directionally solidified $BaCe_{0.8}Y_{0.2}O_{3-\delta}$.

SrCe$_{0.9}$Y$_{0.1}$O$_{3-\delta}$

Phase intercellular:
• Low in Ce
• High in Al
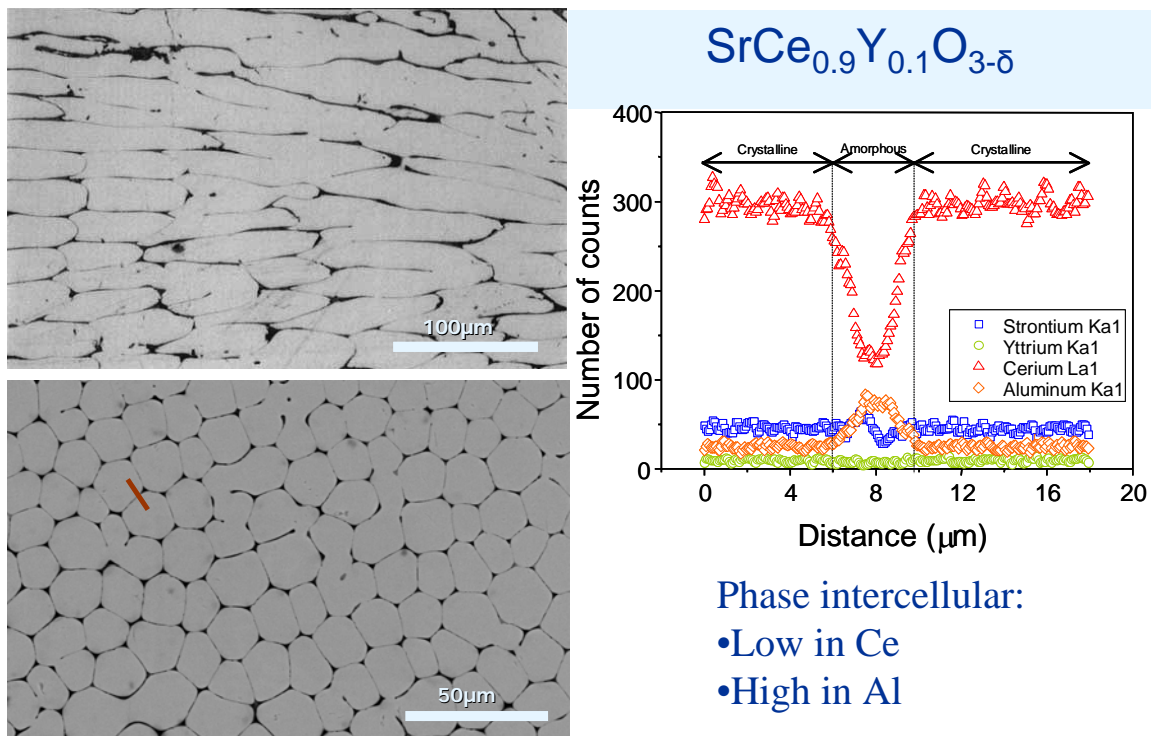
Figure 11 – Typical micorstructure of the directionally solidified HTPC. A typical composition profile of the intercellular phase is also included.

TEM - SrCe$_{0.9}$Y$_{0.1}$O$_{3-\delta}$
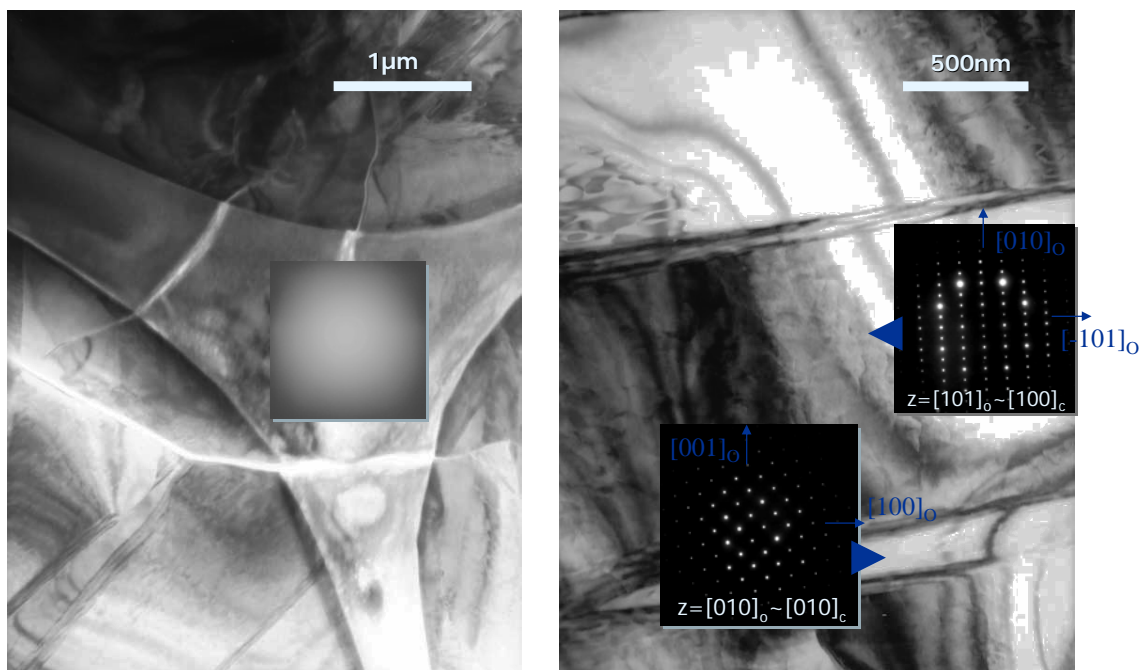
Figure 12 – Transmission electron microscopy micrographs of the directionally solidified HTPC.
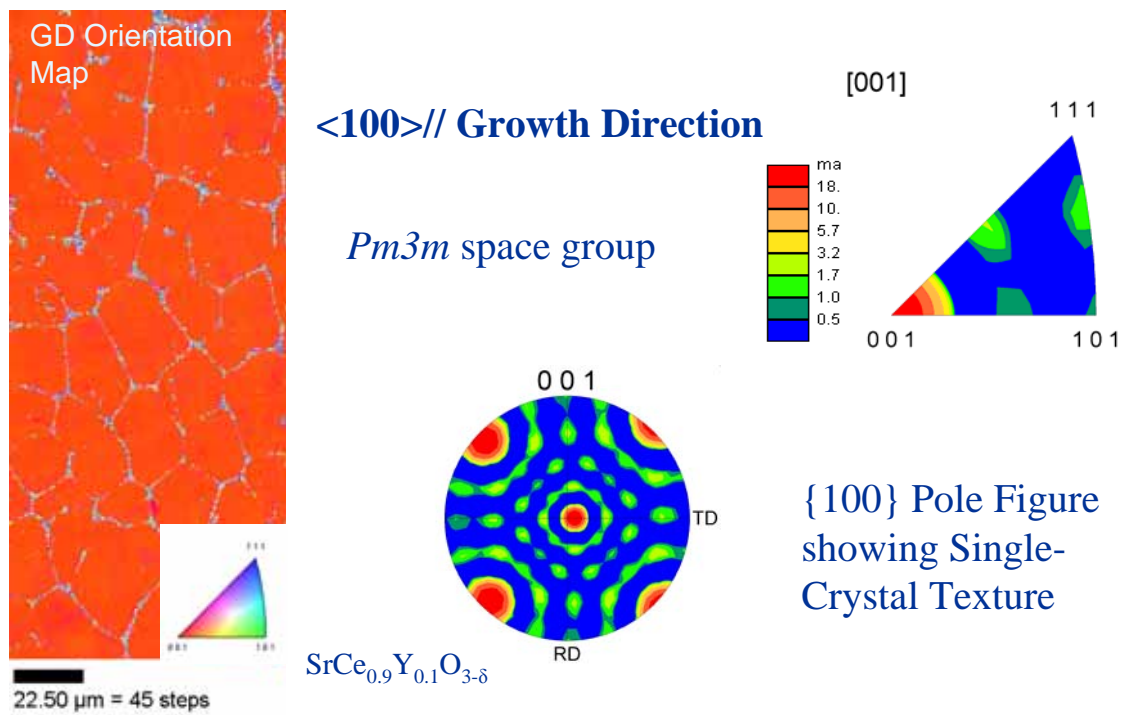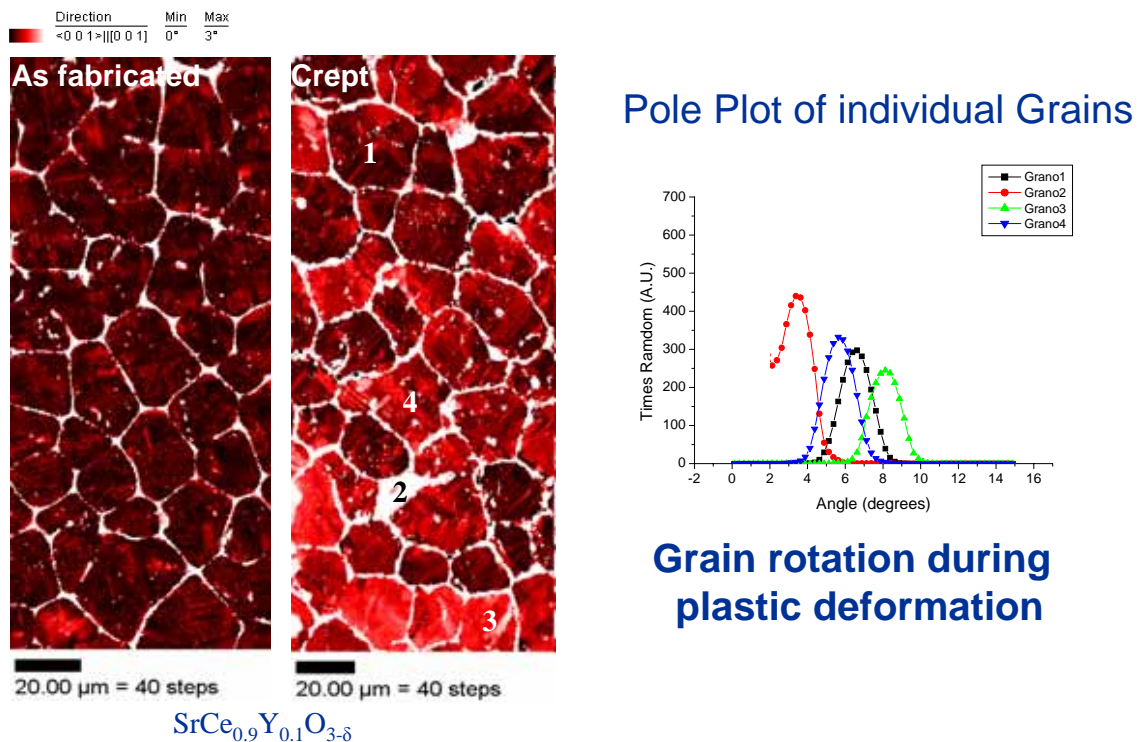
Figure 13 – Distribution of the crystallographic orientation on directionally solidified HTPC, measured by electron back scattering diffraction.
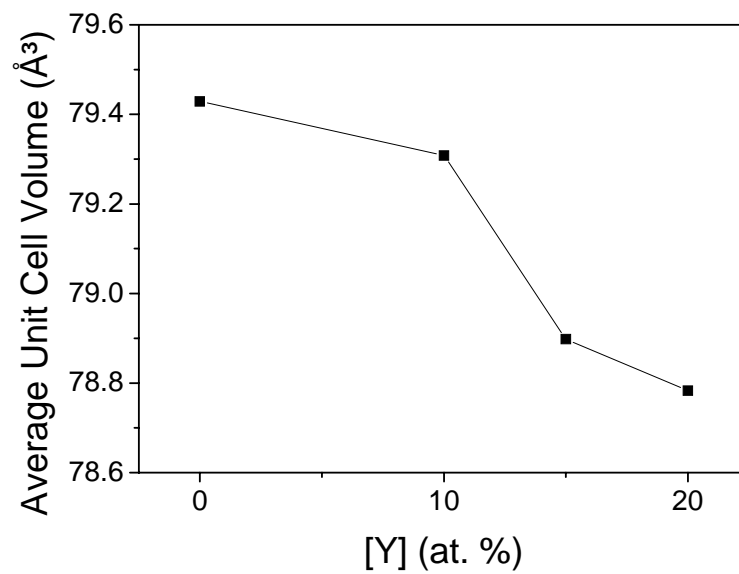
Figure 14 – Plot of the average unit cell versus the dopant content
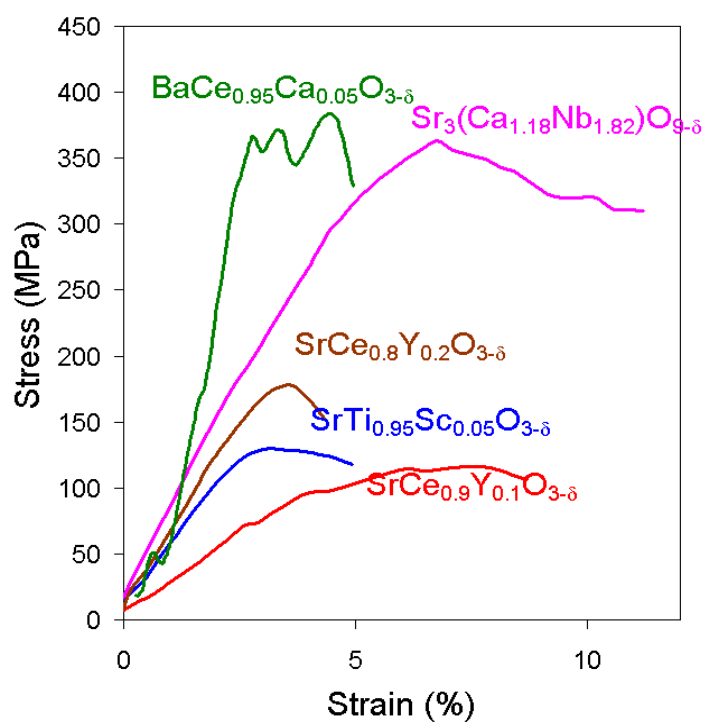
Figure 15 – Plot of stress versus strain for directionally solidified HTPC at 1300 $^{\circ}$C.
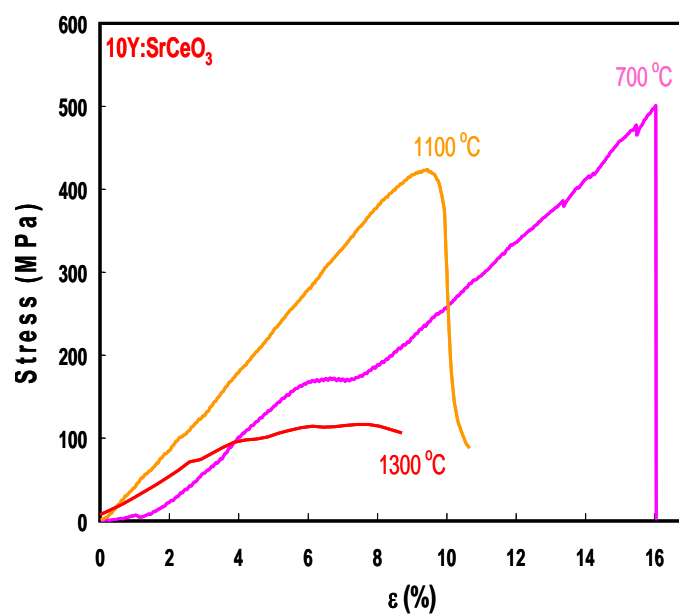
Figure 16 - Plot of stress versus strain for directionally solidified HTPC at different temperatures.
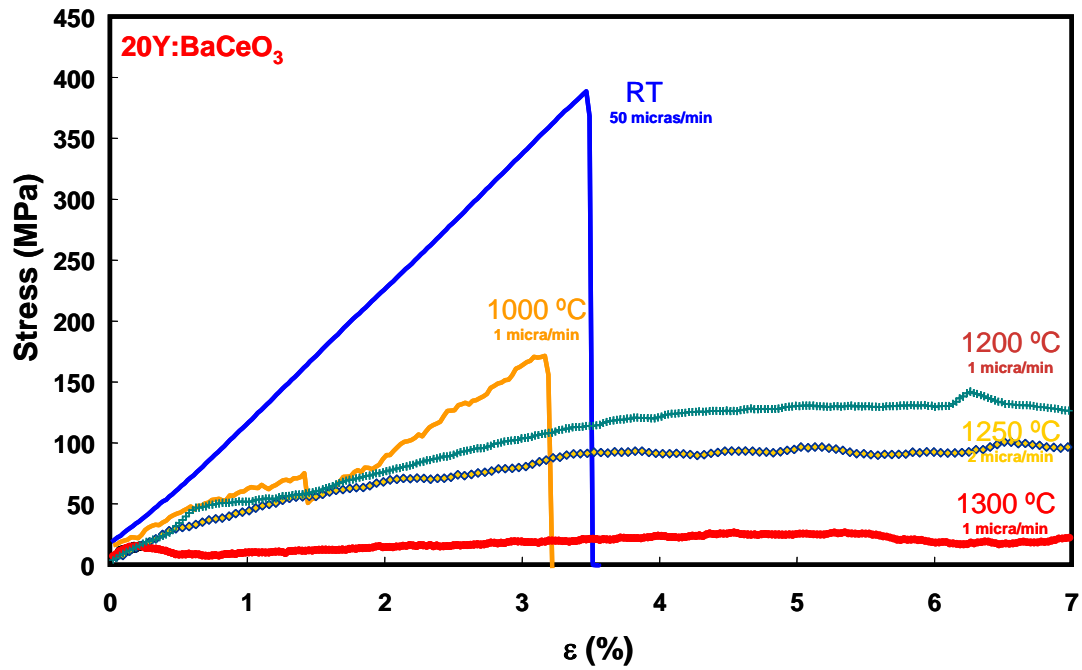
Figure 17 - Plot of stress versus strain for polycrystalline HTPC at different temperatures.
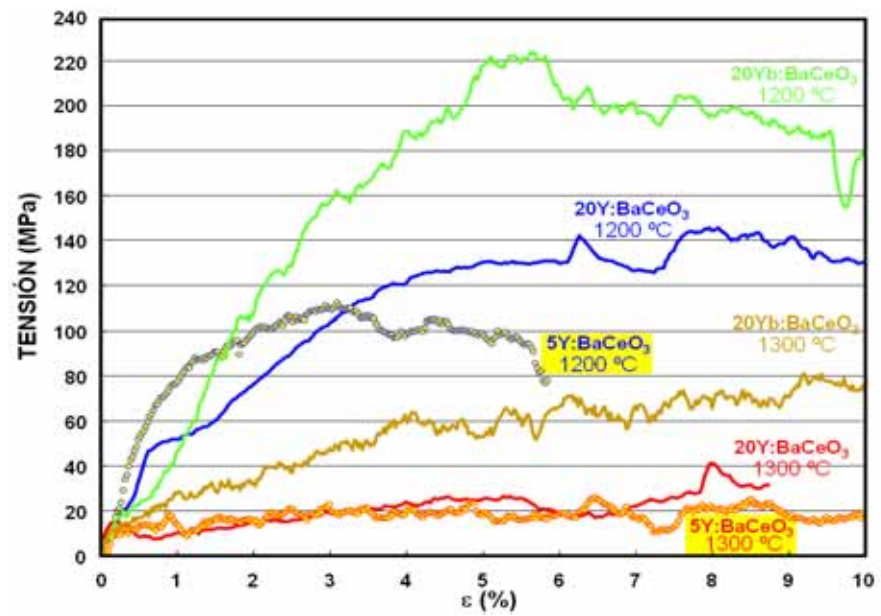
Figure 18 – Plot of stress versus strain for polycrystalline HTPC at high temperature.
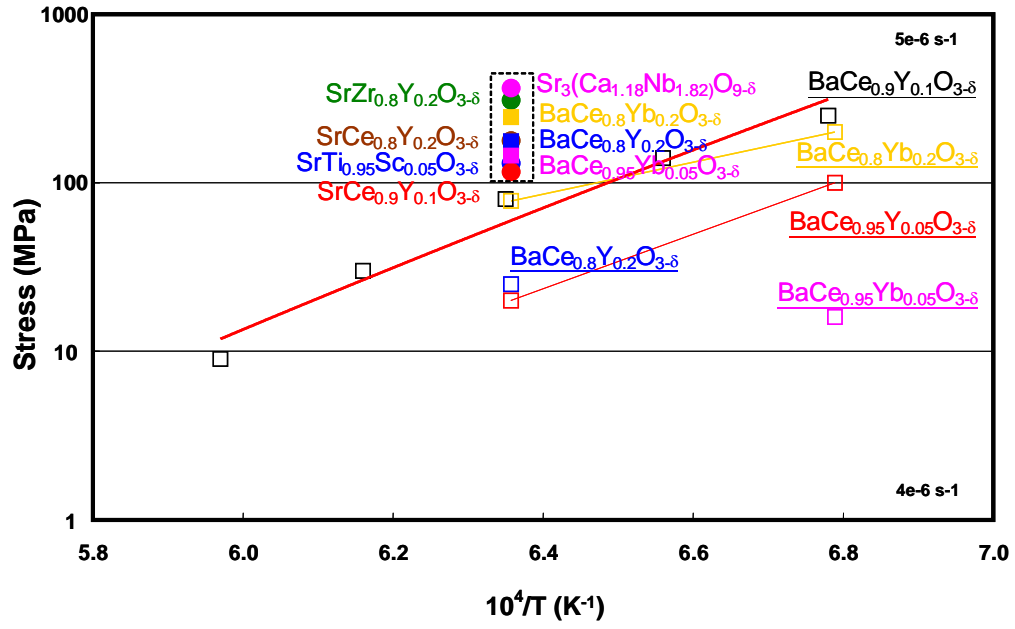
Fig 19 – Plot of the strength as a function of temperature for directionally solidified (solid symbols) and polycrystalline HTPC.
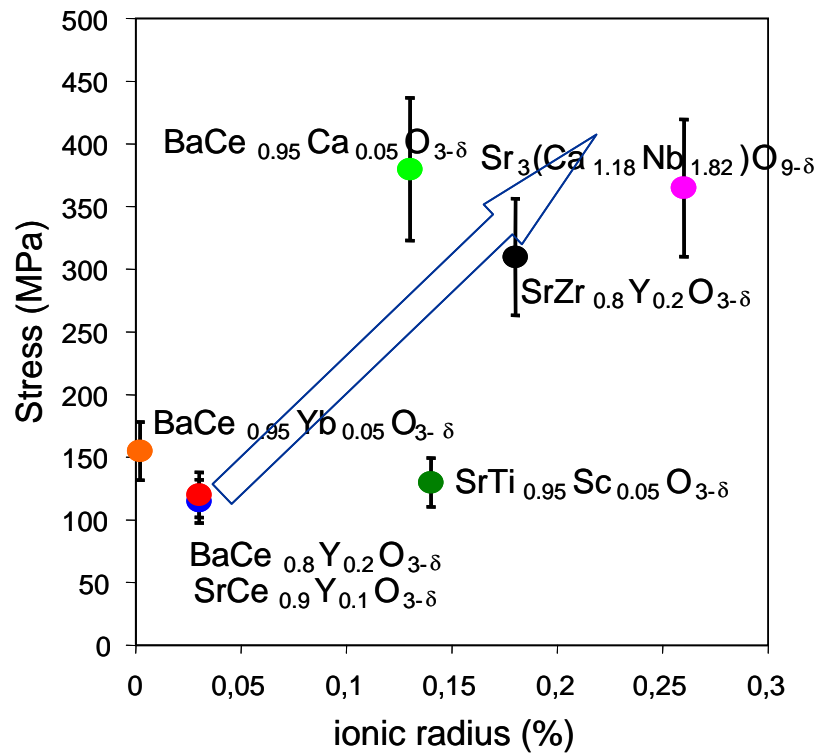
Figure 20. Representation of the strength vs. difference of ionic radius (Ce^{4+}-dopant) of melt grown HTPC tested to 1300ºC.
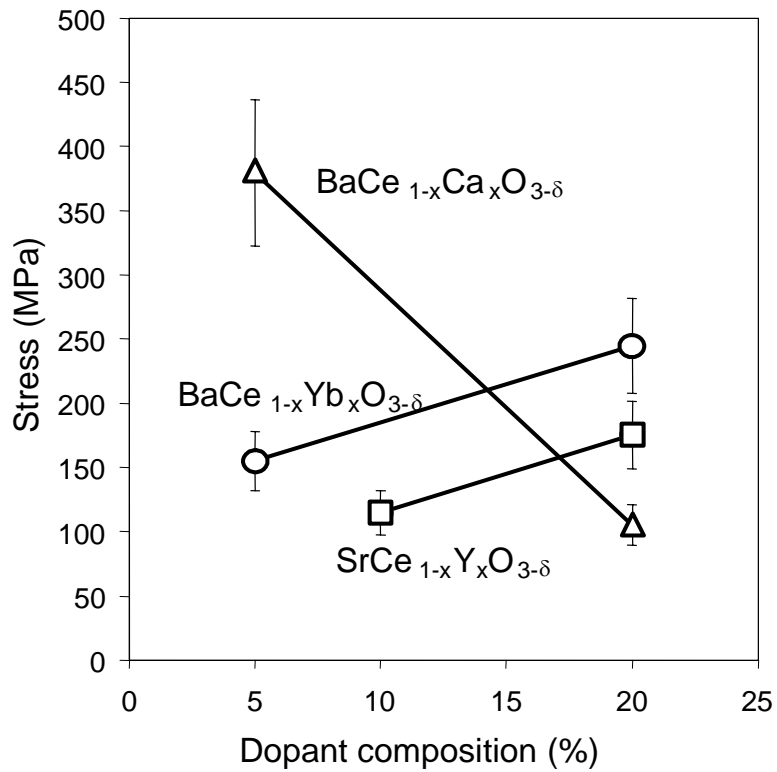
Figure 21. Representation of the strength vs. dopant concentration of melt grown HTPC tested to 1300ºC.

$Sr_3Ca_{1.18}Nb_{1.82}O_{9-\delta}$ 1300ºC

$\dot{\varepsilon}(10^{-7}s^{-1})$

2.48   4.30 1.49   3.29   1.37   3.31   1.37   3.31   0.83

$\varepsilon(t)$
$\sigma(t)$

Ar
Air

Steady state creep

Higher creep resistance than polycrystals (x 20-100)

Creep controlled by a viscous intercellular phase

Increase of σ o T

$$\frac{d\varepsilon_z}{dt} = \frac{\sigma_z}{\eta}\left[\frac{1}{\gamma\left(\frac{h}{d}-\varepsilon_z\right)^3} + \frac{4}{\left(\frac{2h}{d}+\varepsilon_z\right)^3}\right]^{-1}$$

Martinez et al.
Acta Materialia
51 [11] (2003) 3259
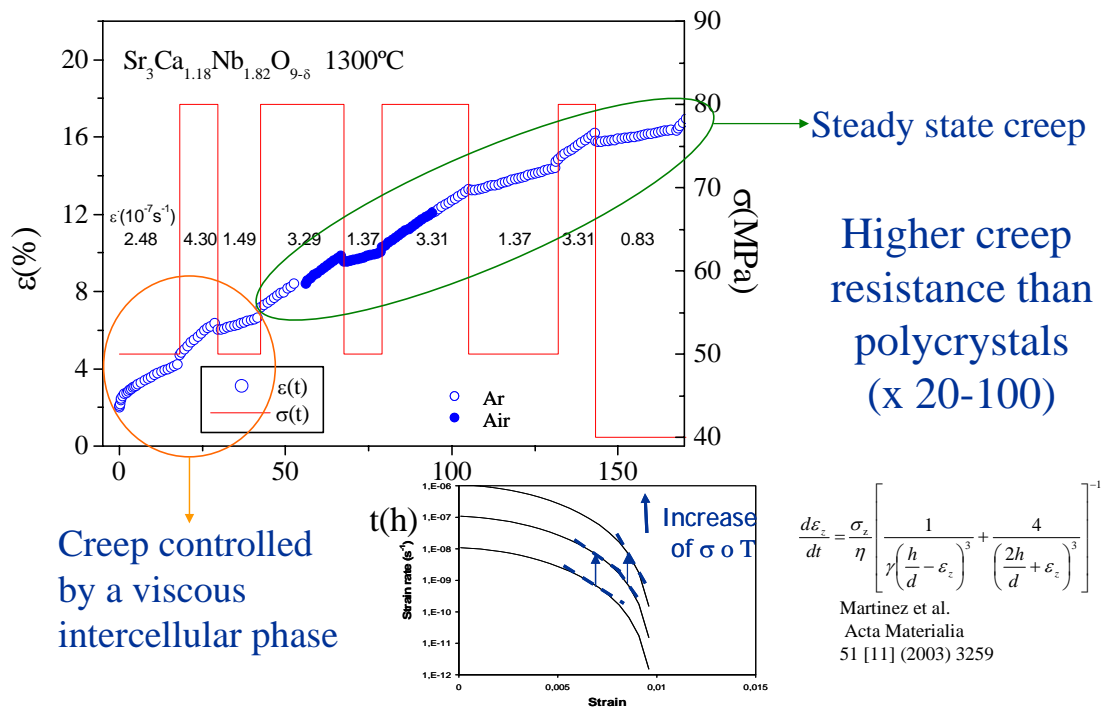
Figure 22 – Typical creep curve for directionally solidified HTPC. See text for further discussion.

Direction   Min   Max
<0 0 1>||[0 0 1]   0°   3°

As fabricated

Crept

Pole Plot of individual Grains

Grano1
Grano2
Grano3
Grano4

Grain rotation during plastic deformation

20.00 µm = 40 steps

20.00 µm = 40 steps

$SrCe_{0.9}Y_{0.1}O_{3-\delta}$

Figure 23 - Distribution of the crystallographic orientation on directionally solidified HTPC after plastic deformation, measured by electron back scattering diffraction.
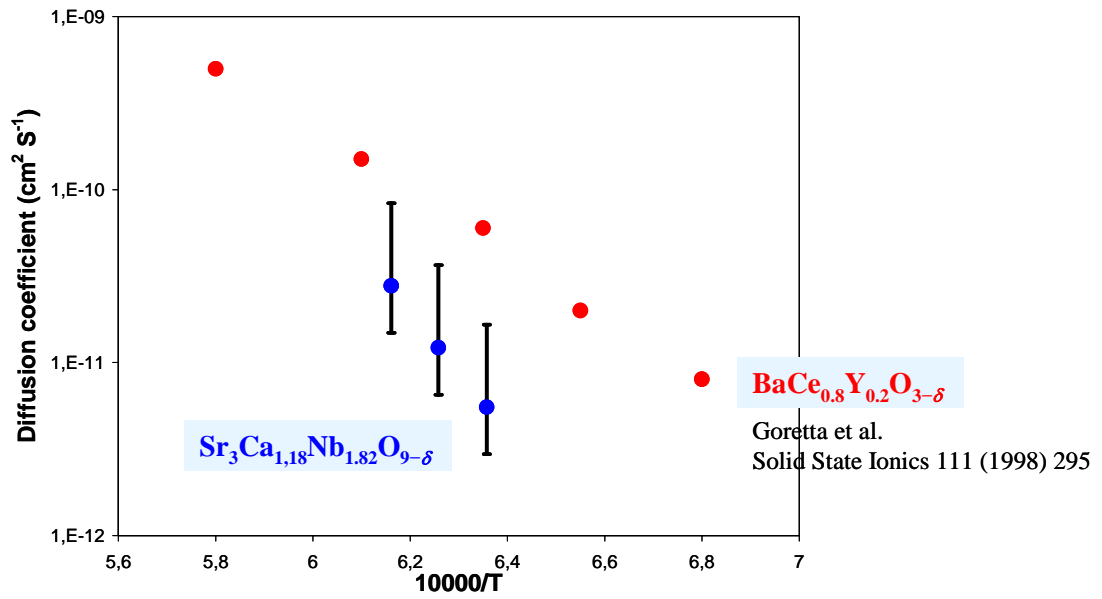
Figure 24 - Estimated diffusion coefficient obtained from creep data for $Sr_3Ca_{1.18}Nb_{1.82}O_{9-}$ compared to data obtained for $BaCe_{0.8}Y_{0.2}O_{3-\delta}$
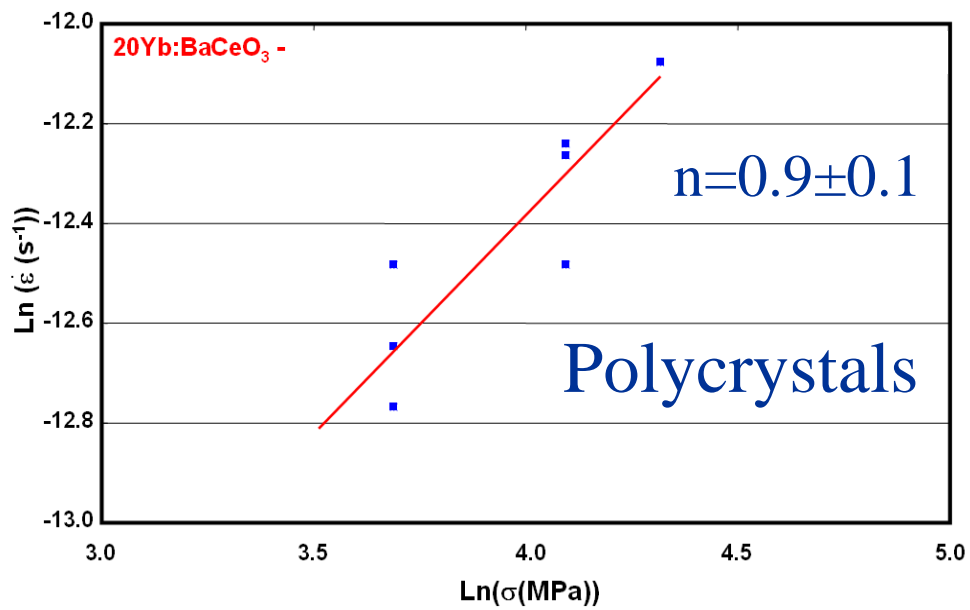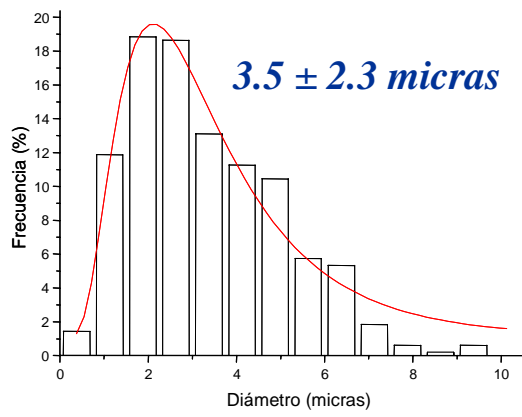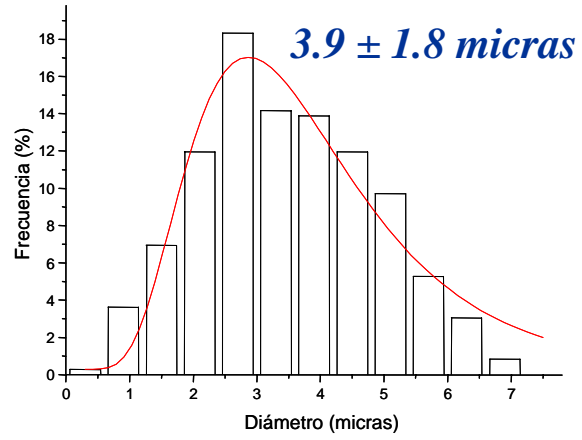

Figure 25 – Plot of strain rate vs. stress used to determine of the stress exponent n, in polycrystalline HTPC.
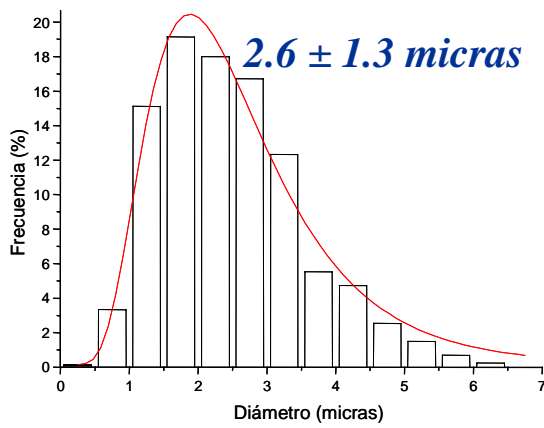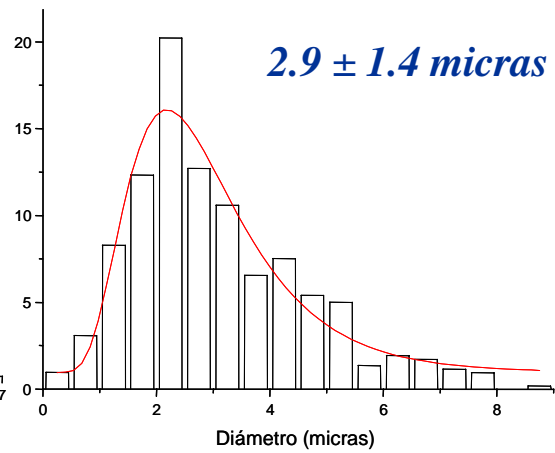
A

20Yb:BaCeO₃ as produced

20Yb:BaCeO₃ deformed

20Y:BaCeO₃ as produced
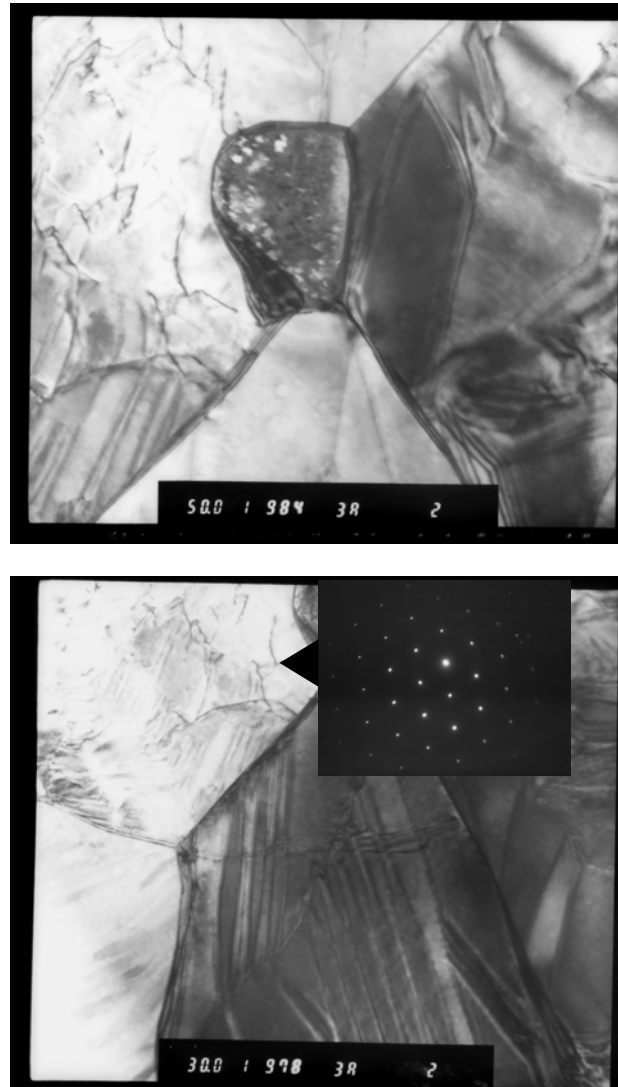

20Y:BaCeO₃ deformed

B

20Y:BaCeO$_3$ deformed

Figuer 26 – A) Grain size distribution before and after plastic deformation in polycrystalline HTPC. B) Transmission electron microscopy micrographs of the grains after plastic deformation.
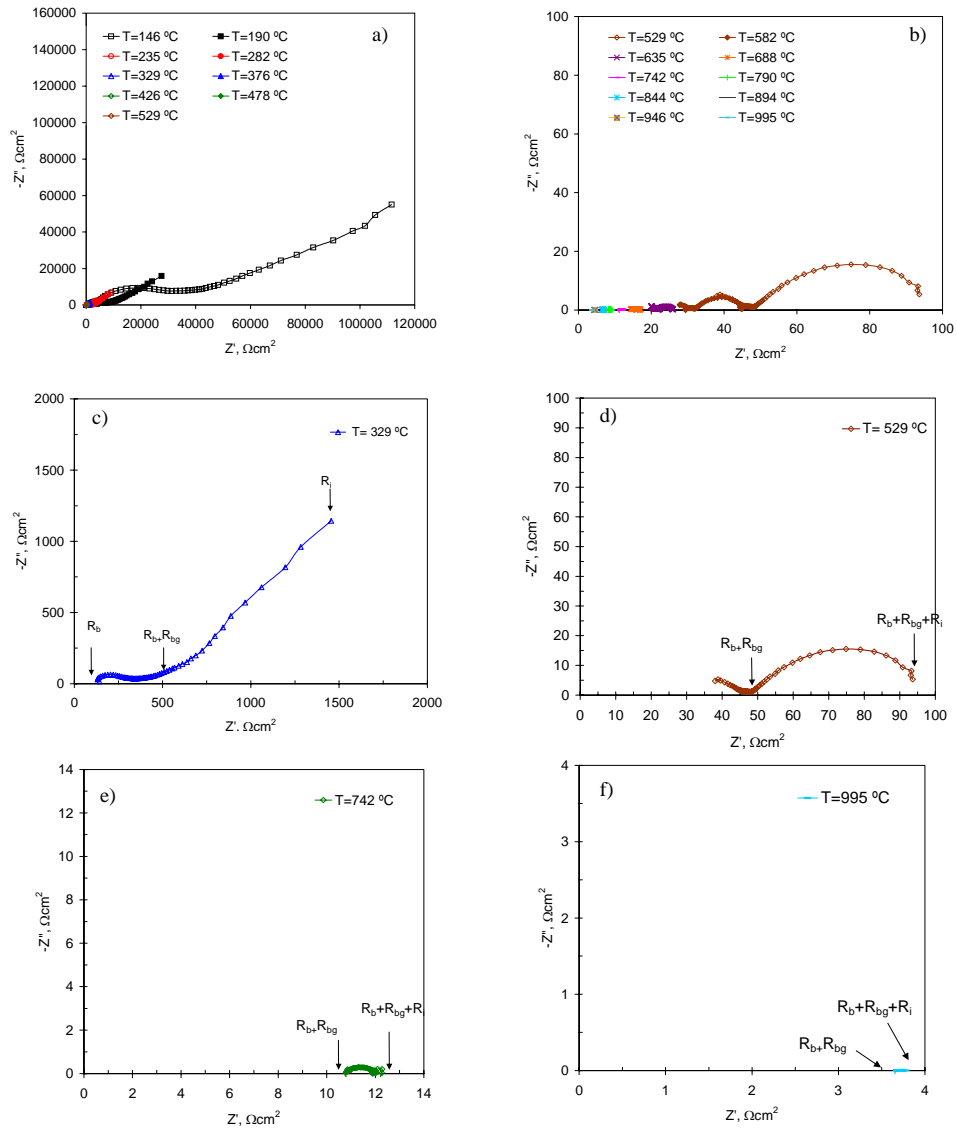
Figure 27. Impedances of the compound 20Y:BaCeO$_3$ measured to different temperatures: a) 146-529 °C; b) 529-995 °C; c) 329 °C; d) 529 °C; e) 742 °C; f) 995 °C.
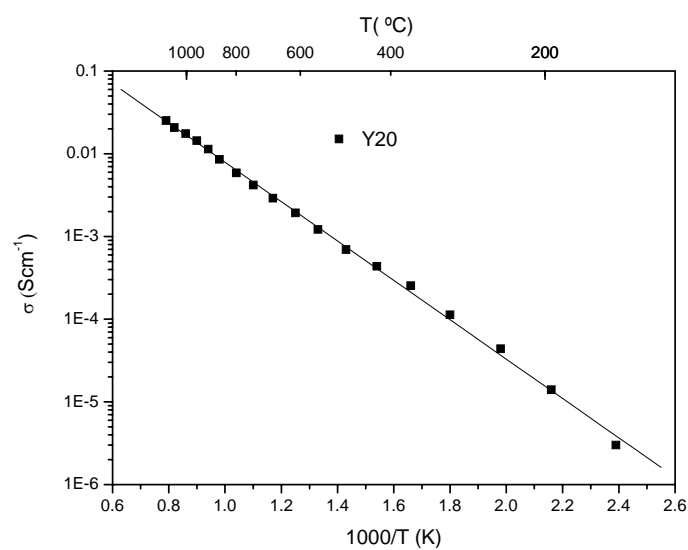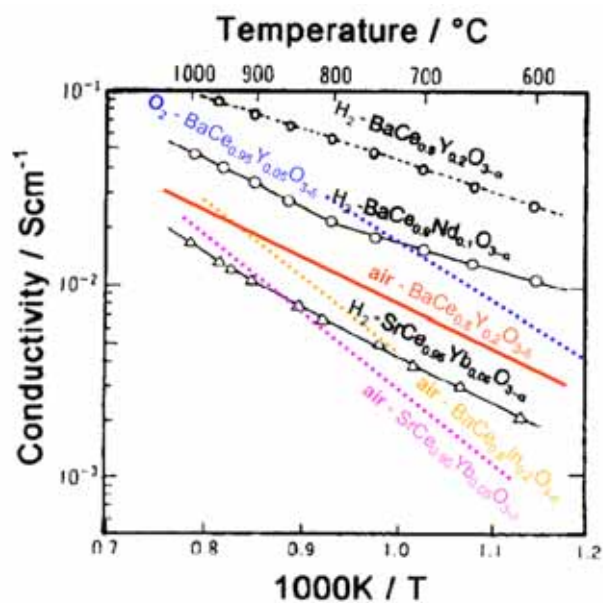
Figure 28. Ionic conductivity of the electrolyte 20Y:BaCeO$_3$.

Figure 29. Ionic conductivity of the electrolyte 20Y:BaCeO$_3$ (in red), plotted with
literature data.